Hindawi Publishing Corporation
Shock and Vibration
Volume 2016, Article ID 6031893, 21 pages
http://dx.doi.org/10.1155/2016/6031893

Research Article

Research on Aerodynamic Noise Reduction for High-Speed Trains

Yadong Zhang, Jiye Zhang, Tian Li, Liang Zhang, and Weihua Zhang

State Key Laboratory of Traction Power, Southwest Jiaotong University, Chengdu 610031, China

Correspondence should be addressed to Tian Li; litian2008@home.swjtu.edu.cn

Received 3 June 2016; Accepted 18 August 2016

Academic Editor: Salvatore Russo

A broadband noise source model based on Lighthill's acoustic theory was used to perform numerical simulations of the aerodynamic noise sources for a high-speed train. The near-field unsteady flow around a high-speed train was analysed based on a delayed detached-eddy simulation (DDES) using the finite volume method with high-order difference schemes. The far-field aerodynamic noise from a high-speed train was predicted using a computational fluid dynamics (CFD)/Ffowcs Williams-Hawkings (FW-H) acoustic analogy. An analysis of noise reduction methods based on the main noise sources was performed. An aerodynamic noise model for a full-scale high-speed train, including three coaches with six bogies, two inter-coach spacings, two windscreen wipers, and two pantographs, was established. Several low-noise design improvements for the high-speed train were identified, based primarily on the main noise sources; these improvements included the choice of the knuckle-downstream or knuckle-upstream pantograph orientation as well as different pantograph fairing structures, pantograph fairing installation positions, pantograph lifting configurations, inter-coach spacings, and bogie skirt boards. Based on the analysis, we designed a low-noise structure for a full-scale high-speed train with an average sound pressure level (SPL) 3.2 dB(A) lower than that of the original train. Thus, the noise reduction design goal was achieved. In addition, the accuracy of the aerodynamic noise calculation method was demonstrated via experimental wind tunnel tests.

1. Introduction

With the high running speeds of high-speed trains, problems that can be neglected at low speeds become sufficient to limit improvements in train speed [1, 2]. Shen [3] notes that the dynamic environment of an ordinary train depends mainly on machinery and electricity. By contrast, the dynamic environment of a high-speed train depends mainly on aerodynamic forces; therefore, aerodynamic noise becomes the greatest limitation. Thompson et al. [4] also indicate that noise pollution has become the most critical environmental problem along high-speed railways. Aerodynamic noise rapidly increases with increasing running speeds, becoming the main noise source for high-speed trains. Indeed, the sound power of aerodynamic noise grows as the 6th power of the running speed [5]. Noise that exceeds standard requirements has become one of the main limiting factors of train speeds, restricting the sustainable development of high-speed railways. Thus, studies of the characteristics of aerodynamic noise, low-noise designs, and noise reduction can facilitate the further development of high-speed trains.

In current research on aerodynamic noise, the location and classification of the noise sources and related low-noise design principles are the main research focus. Talotte [1], Nagakura [6], and Kitagawa and Nagakura [7] report that the main aerodynamic noise sources for high-speed trains are as follows: the pantograph, the first bogie, the power head nose, the head cowcatcher, the train head, the train tail, the train windows, the train doors, the inter-coach spacings, and the bogie skirt boards. These aerodynamic noise sources can be classified into two types. The first type corresponds to noise radiated by a steady flow structure. For example, the steady vortex shedding immediately behind the pantograph can generate significant aerodynamic noise, which strongly contributes to the overall noise. Moreover, certain cavity structures on the surfaces of high-speed trains can also generate aerodynamic noise. The other type of noise source refers to noise emitted by turbulent fluctuations, which occur

mostly in the turbulent boundary layer near the surface of a high-speed train or at locations where flow separations occur.

Reducing the aerodynamic noise of high-speed trains requires reducing the noise from the main noise sources. The significant current collection between the pantograph and catenary set on top of a high-speed train, because of its complex structure, strongly affects the train's aerodynamic performance. Rough areas on the train severely disturb the airflow at high speeds, thereby generating complex flow separation and vortex shedding phenomena; the resulting powerful fluctuations in air pressure in the far field translate into aerodynamic noise. This source can be predominant in case of the high-speed train is running behind a ~4 m high noise barrier as the pantograph is higher than the noise barrier. King III [8] presented a method of using dipole sources to describe the aerodynamic noise induced by the vortex shedding of a pantograph and discovered a linear relationship between the far-field aerodynamic noise and the logarithm of the speed. Noger et al. [9] performed wind tunnel experiments on a 1 : 7 scale mock-up both with and without pantographs and identified the pantograph fairing as an important aerodynamic noise source. Sueki et al. [10] conducted full-scale and wind tunnel measurements of a PS207 pantograph (as installed on the Series E2-1000 Shinkansen) equipped with porous materials and demonstrated that a noise reduction of 1.9 dB(A) at 360 km/h could be achieved, with a significant noise reduction of 5 dB at the 1/3 octave band centre frequency at 250 Hz. The results show that the material properties of a pantograph significantly influence its aerodynamic noise. Lee and Cho [11], Ikeda et al. [12], and Kurita [13] developed an optimized pantograph structure and tested the proposed PS207 pantograph in a noise reduction experiment, in which the noise reduction effects of a low-noise panhead structure in combination with the new pantograph type were studied in wind tunnel tests. Yu et al. [14] also considered the effect of a pantograph fairing installed on the roof of a train. They found that if the fairing consisted of two sideward baffles acting as noise barriers, then a noise reduction of 3 dB could be achieved.

The bogie is one of the main aerodynamic noise sources for a high-speed train. However, because of the complex structure and disordered distribution of the flow field around a vortex, bogie aerodynamic noise is poorly understood. In numerical calculations, only minimal noise reduction can be achieved if the bogie structure is excessively simplified or if a simplified small-scale model is used. Wakabayashi et al. [15] and Kurita et al. [16] performed noise tests on a FASTECH360 S train with full skirt boards for all bogies and found that the noise from the lower part of the train was reduced by approximately 1 dB compared with a Series E2-1000 train. Based on a delayed detached-eddy simulation (DDES) and the Ffowcs Williams-Hawkings (FW-H) equation, the distribution patterns of the dipole and flow-field characteristics of a simplified 1 : 10 scale bogie model including a wheel set and bogie frame were predicted and investigated by Zhu et al. [17]. The accuracy of the numerical calculations was verified via wind tunnel experiments. Zhang et al. [18] presented a numerical method of using dipole sources to describe the aerodynamic noise induced by the trailer car bogie and discovered that the far-field aerodynamic noise of the trailer car bogie was broadband noise that has noise directivity, attenuation characteristic, and amplitude characteristic.

A low-noise structure for the CRH3 train was designed using both a nonlinear acoustic solver and the FW-H equation by Sun et al. [19]. Their results showed that the use of smooth transitions for head windows and streamline positions and the use of a streamlined design for the head cowcatcher could reduce the near-field noise by 7 dB(A) and 14 dB(A), respectively, compared with the original model. Yamazaki et al. [20] found that the inter-coach spacing is also a major noise source for high-speed trains by conducting wind tunnel experiments and field tests using a 1 : 5 scale Shinkansen train model.

Currently, research on aerodynamic noise related to high-speed trains is primarily conducted through experiments and numerical simulations. The former predominantly consist of wind tunnel experiments based on reduced-scale models and field tests based on full-scale models. However, field tests are time consuming, require high levels of manpower and resources, and are subject to numerous restrictions in terms of simulating real-world conditions. Meanwhile, wind tunnel experiments based on reduced-scale models must satisfy strict test conditions (such as conditions on the Reynolds number and the turbulence intensity of the boundary layer). Therefore, with the development of modern computers, numerical simulations have gradually become an accepted means of predicting aerodynamic noise. Compared with experiments, numerical simulations offer greater controllability and better facilitate the calculation of aerodynamic noise. Moreover, they allow noise to be predicted under different flow conditions and for different parameters values.

As an extension of the investigations discussed above, the study presented in this paper addresses the aerodynamic noise induced by full-scale high-speed trains, the characteristics of the far-field aerodynamic noise, and the study of noise reduction. To obtain high-quality results for high-speed trains through numerical simulations, a highly detailed geometry was used, and the unsteady simulations were performed at full scale. An aerodynamic noise model was established for a full-scale high-speed train, including three coaches with six bogies, two inter-coach spacings, two windscreen wipers, and two pantographs (with the first pantograph folded and the second pantograph lifted on the middle coach). The steady-state RNG k-ε turbulence model and broadband noise sources were used for a preliminary study of the aerodynamic noise sources. Then, by combining the model with an unsteady DDES and the FW-H equation, the far-field aerodynamic noise was analysed. Based on the studies described above, an accurate distribution of the aerodynamic noise sources on the surface of the high-speed train and the far-field distribution characteristics were obtained. Low-noise design principles were developed and noise reduction analyses were conducted for the main aerodynamic noise sources. To reduce noise, it is essential to consider the two main operation orientations of a pantograph, different pantograph fairing structures, different pantograph fairing installations, different choice of which pantograph is lifted in double pantograph, the presence of diaphragm plates in

inter-coach spacings, and the effects of bogie skirt boards. Wind tunnel tests were performed to thoroughly verify the correctness of the numerical analysis method used in this paper.

2. Numerical Fluid Analysis and Aerodynamic Noise Analysis Methods

2.1. Delayed Detached-Eddy Simulation. Computational fluid dynamics (CFD) was used to calculate the induced airflow around the train, and computational aeroacoustics (CAA) was applied to predict the aerodynamic noise [21]. In typical CFD turbulence models, a detached-eddy simulation (DES) model is more universal than an unsteady Reynolds-averaged Navier-Stokes (URANS) model or a large eddy simulation (LES) model and saves significant computation time compared with direct numerical simulation (DNS) or the LES approach [22]. Therefore, dynamic fluid flow characteristics can be obtained using a DES model, whereas a URANS model with empirical parameters can capture only unsteady mean-flow structures and is therefore unable to provide the detailed unsteady flow information required for noise calculations [4]. DNS is considered to be a simple research tool that is suitable for scenarios with low Reynolds numbers [22, 23]. Although LES is much cheaper than DNS, it still requires a significant number of grid points, especially near solid boundaries, and must be run with very small time steps, which means that it is not a practical option for most industrial applications [24]. Based on the above considerations, a DES turbulence model is clearly the most suitable means of aerodynamic noise prediction for high-speed trains at present. A refinement of DES is the delayed detached-eddy simulation (DDES) approach, which was developed to avoid grid-induced separation and to preserve URANS modelling throughout the boundary layer [25]. There are two popular types of DDES model, one based on the simple *Spalart-Allmaras* model and one based on the SST *k-omega* model, of which the latter is used in this paper.

2.2. Ffowcs Williams-Hawkings Acoustic Analogy. The acoustic analogy method is widely used in CAA. The theory was first presented by Lighthill [26] and was extended by Curle [27]; subsequently, Ffowcs Williams and Hawkings [28] developed the FW-H equation. This differential equation [28] is given as follows:

$$\left(\frac{1}{c_0}\frac{\partial^2}{\partial t^2} - \frac{\partial^2}{\partial x_i^2}\right) p' = \frac{\partial}{\partial t}\left[\rho v_n \delta(f)\nabla f\right] - \frac{\partial}{\partial x_i}\left[n_i p \delta(f)\nabla f\right] + \frac{\partial^2}{\partial x_i \partial x_j}\left[T_{ij} H(f)\right], \quad (1)$$

$$T_{ij} = \rho u_i u_j + P_{ij} - c_0^2 \rho \delta_{ij}, \quad (2)$$

where ρ is air density, p air pressure, p' sound pressure, n_i normal direction, c_0 constant speed of sound in the undisturbed medium, u_i time-averaged velocity in the i direction, u_j time-averaged velocity in the j direction, v_n surface velocity component normal to the surface, T_{ij} Lighthill stress tensor, P_{ij} fluid compressive stress tensor, $\delta(f)$ Dirac delta function, and $H(f)$ Heaviside function.

Based on the near-field unsteady flow data obtained from CFD calculations, the FW-H equation can be used to predict the sound generated from equivalent acoustic sources. The right-hand side of (1) includes contributions from the monopole sources, dipole sources, and quadrupole sources. When a high-speed train runs at a certain speed (up to a speed of 400 km/h, at a Mach number ($M = u/c_0$) of 0.33), monopole sources need not be considered because the train's surfaces can be regarded as arbitrary rigid bodies and the pulsating volume approaches zero [19, 21]. The authors of [29] note that the intensity ratio of between quadrupole and dipole sources intensities in the flow field is proportional to M^2. Because high-speed trains still operate at a sufficiently low speed that the noise intensity of quadrupole sources is far less than that of dipole sources, quadrupole sources can also be ignored. Therefore, the problem of the far-field aerodynamic noise induced by dipole-type sources on high-speed trains is considered in this work.

3. Evaluation Criteria for Low-Noise Design

In this paper, high-speed railway noise is evaluated in terms of the A-weighted equivalent continuous sound pressure level (SPL) ($L_{pAeq,T}$). According to the definition given in the international standard ISO3095-2013 [30] for the noise testing of high-speed trains, $L_{pAeq,T}$ is calculated as follows:

$$L_{pAeq,T} = 10\lg\left(\frac{1}{T}\int_0^T \frac{p_A^2(t)}{p_0^2}dt\right), \quad (3)$$

where T is a time interval, $p_A(t)$ is the instantaneous A-weighted SPL, and p_0 is the reference sound pressure of 20 μPa.

The fast Fourier transform is used to transform the sound pressure at far-field evaluation points into the frequency domain, where they are revised using the A-weighted frequency-domain table [31]. Then, the inverse Fourier transform is used to transform the frequency-domain sound pressures into the time domain to obtain $p_A(t)$ for the evaluation points. Finally, the $L_{pAeq,T}$ values for the evaluation points are calculated using (3). Two derived quantities based on $L_{pAeq,T}$ are used as indices for aerodynamic noise assessment: the max $L_{pAeq,T}$ (L_{max}) and the average $L_{pAeq,T}$ (L_{pm}). According to the principle of energy superposition, L_{pm} is expressed in the following form:

$$L_{pm} = 10\lg\left(\frac{1}{m}\sum_{i=1}^{m} 10^{0.1 L_{pAeq,Ti}}\right), \quad (4)$$

where $L_{pAeq,Ti}$ ($i = 1, 2, \ldots, m$) denotes the $L_{pAeq,T}$ value for the ith evaluation point and m is the number of noise evaluation points.

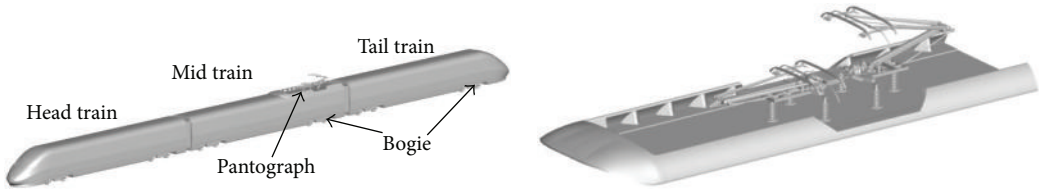

Figure 1: The geometric model: (a) the full vehicle and (b) the original pantograph fairing Dlz1.

Table 1: Mesh configurations and computational results.

Mesh	Mesh points (million)	First layer thickness (mm)	Number of prism layers	Minimum size (mm)	Stretching ratio	L_{pm} (dB(A))
1	56.32	0.1	8	2	1.2	88.5
2	64.78	0.1	12	2	1.2	86.9
3	70.03	0.1	8	1	1.2	87.7

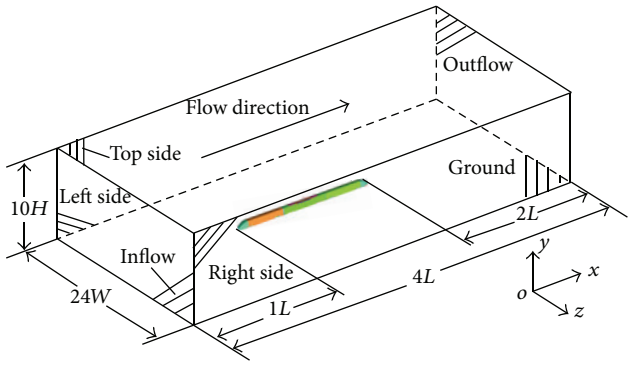

Figure 2: Computational flow-field domain.

4. The Aerodynamic Noise Calculation Model

4.1. Computational Model. A specific type of full-scale high-speed train was selected as the research object for this study. This train is equipped with three coaches, namely, the head train, mid train, and tail train, and includes six bogies, two windscreen wipers, two inter-coach spacings, and a pantograph fairing and two pantographs on the mid train (the first pantograph is folded, and the second is lifted; see Figure 1(a)). The vehicle parameters are as follows: the model has full-scale length, width, and height dimensions of 80.89 m, 3.36 m, and 3.86 m, respectively. The head train and tail train are both 27.12 m in length, and the shape of the tail train is the same as that of the head train. The length of the mid train is 25 m. The length of the streamlined head is 5.48 m, the horizontal maximum cross-sectional area of the train is 12.16 m^2, and the slenderness ratio is 1.63. The original pantograph fairing design is denoted by the code Dlz1 (see Figure 1(b)).

4.2. Computational Domain and Boundary Conditions. The computational domain for the high-speed train is depicted in Figure 2. The model dimensions are approximately $L = 80.89$ m, $H = 3.86$ m, and $W = 3.36$ m along the x-, y-, and z-directions, respectively. The computational domain has dimensions of $4L \times 10H \times 24W$. The distance from the nose of the head train to the flow entrance is $1L$, the distance from the nose of the tail train to the flow exit is $2L$, and the height between the floor of a coach and the ground is 0.376 m.

The inflow boundary is assigned a velocity inlet condition corresponding to a flow speed of 69.4444 m/s (equivalent to a running speed of 250 km/h). The outflow boundary is assigned a pressure outlet condition corresponding to a gauge pressure of 0 Pa, and the reference pressure is set to 1 atm. The right, left, and top sides are defined as symmetric boundaries. A no-slip wall boundary condition is applied at the surface of the train. To achieve an analogue ground effect, the ground can be defined as a slipping surface, with a speed equal to the running speed of the train.

4.3. Grid-Independent Validation. Grid-independent validation was performed using different numbers of hexahedral meshes combined to form a prism mesh near the surface of the train, with a more highly refined mesh in the wake regions of the tail train and the pantograph to assess the influence of different spatial meshes on the calculation results. With the thickness of the first prism layer defined to satisfy the requirement of the wall function [32], three meshes configurations were considered in the present study. The parameters of the three mesh configurations and the corresponding computational results are listed in Table 1. The L_{pm} value for the entire train obtained using the first mesh configuration is only 1.6 dB(A) higher than that obtained using the second mesh configuration and 0.8 dB(A) higher than that obtained using the third mesh configuration. Therefore, it can be concluded that the mesh configuration has a minimal influence on the computational results. Thus, all flow-field calculations presented in this paper were performed using the configuration with the fewest mesh points to reduce the computation time. The distribution of the spatial grids is illustrated in Figure 3.

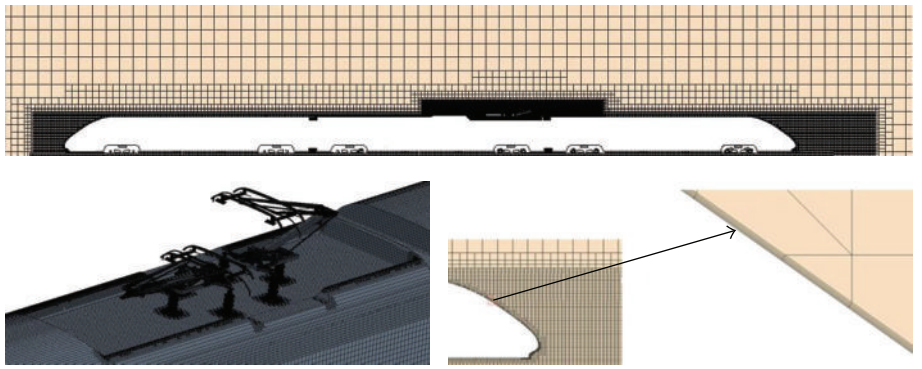

Figure 3: Distribution of the spatial grids.

Table 2: Main modelling schemes adopted for the CFD simulations.

Time dependency	Steady	Unsteady
Turbulence model	RNG k-ε	DDES
Solver	Pressure based	Pressure based
Pressure-velocity coupling	SIMPLEC	PISO
Pressure discretization	Standard	PRESTO!
Momentum discretization	Second-order upwind	Bounded central differencing
Turbulent kinetic energy discretization	QUICK	QUICK
Turbulent dissipation rate discretization	Second-order upwind	Second-order upwind

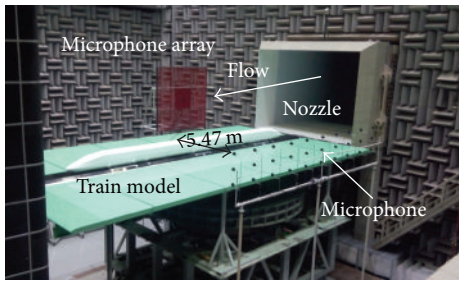

Figure 4: Photograph of the 1 : 8 scale train model in the anechoic wind tunnel.

4.4. CFD Validation. Aerodynamic noise experiments were conducted on a high-speed train in an anechoic test section of a low-turbulence aeroacoustic wind tunnel at the China Aerodynamics Research and Development Centre (CARDC) [33, 34]. In the open test section of the wind tunnel, the width is 5.5 m, the height is 4.0 m, and the length is 14.0 m. When the maximum wind speed reaches 100 m/s, the stream turbulence in the central model region is below 0.05%. When the wind speed reaches 80 m/s in the open test section, the background noise is 76.5 dB(A) at a lateral distance of 7.95 m from the ejector nozzle of the central jet pipe, thereby satisfying the international requirements for advanced aeroacoustic wind tunnel tests (background noise below a lower limit of 75–80 dB(A) in the open test section) [33]. Figure 4 presents a photograph from the test, showing a 1 : 8 scale train model with three coaches and six bogies in the CARDC low-noise wind tunnel in Mianyang, China.

Table 3: Comparisons of L_{pm} between simulations and experiments.

Wind speed (km/h)	160	200	230	250
Wind tunnel test	74.1	80.2	85.4	86.5
Simulation	73.1	78.9	83.9	84.8
Difference	1.0	1.3	1.5	**1.7**

To verify the CFD calculations, the flow field and sound propagation around the three-coach 1 : 8 scale high-speed passenger train model were obtained from a DDES using high-order difference schemes and the FW-H acoustic analogy. A DDES based on the SST *k-omega* model of DDES was used in this study. The commercial CFD program FLUENT, which is based on the finite volume method, was applied to calculate the unsteady aerodynamic noise. To speed up convergence, a steady turbulence computation was performed first and the results of this computation were adopted as the initial unsteady values to solve for the unsteady flow fields. Table 2 summarizes the main modelling schemes adopted for the CFD simulations. The same CFD schemes were applied in all calculations unless otherwise stated.

In this study, the calculation time step for the aerodynamic noise simulations was set to 2×10^{-5} s and the simulated physical time was 0.2 s; these settings ensured characterization of the dynamic behavior with a maximum frequency of 25 kHz and a frequency resolution of 5 Hz.

Table 3 presents the comparisons of the L_{pm} values between the numerical simulations and the experiments, in which the microphones were placed 5.47 m from the centre of

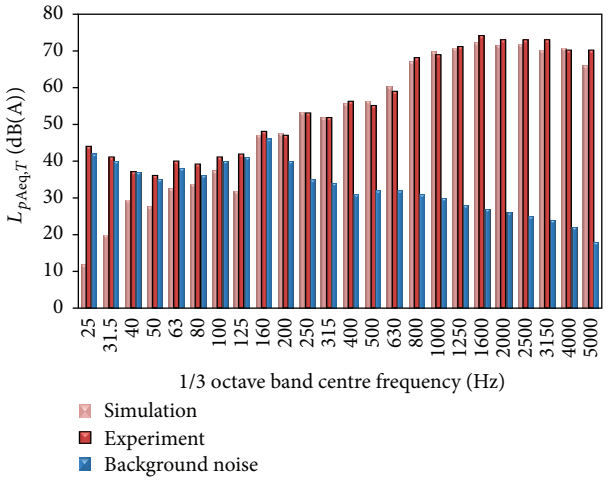

Figure 5: Comparison of simulated and experimental spectra.

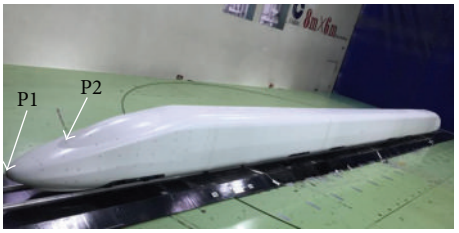

Figure 6: The 1 : 8 scale train model in the aerodynamic force wind tunnel.

Table 4: Comparison of the time-averaged force coefficients between simulation and experiment.

Comparisons	Head train		Mid train		Tail train	
	C_d	C_l	C_d	C_l	C_d	C_l
Simulation	0.145	−0.047	0.071	−0.013	0.162	0.091
Wind tunnel	0.143	−0.045	0.070	−0.012	0.158	0.094
Error (%)	1.40	4.44	1.43	8.33	2.07	3.19

the track and 1 m above the ground and the wind speeds were 160, 200, 230, and 250 km/h. Table 3 shows that the difference between the simulated and experimental values increases with increasing wind speed. The experimental noise levels are systematically higher than the predictions because of the additional noise contributions from reflections from the baffle plate; the numerical L_{pm} value is as much as 1.7 dB(A) lower than the corresponding experimental value.

Figure 5 presents the spectra of the radiated noise at the microphone indicated in Figure 4 (for a wind speed of 160 km/h). Good agreement between the simulated and experimental spectra is observed in terms of both the tonal frequencies of the noise and the spectral shape. Because of the high background noise in the low-frequency range generated by the nozzle itself [12, 24], the results are not accurately predicted by the simulation below 160 Hz. The simulation results reveal that the DDES/FW-H approach is an efficient and high-resolution computational method for aerodynamic noise prediction and can be applied for full-scale computations of the aerodynamic noise generated by a high-speed train.

Wind tunnel experiments for measuring aerodynamic forces were conducted in the second test section at CARDC, which is an 8 × 6 m low-speed wind tunnel with a closed-test section. The dimensions of this test section are approximately $L = 16$ m, $H = 5$ m, and $W = 8$ m. A six-component balance system was applied to measure the drag/lift forces, and the electronic pressure scanners were used to measure the surface pressure on the train. A photograph of the three-coach 1 : 8 scale train model in the aerodynamic force wind tunnel is shown in Figure 6. The model used in the aerodynamic force wind tunnel test was the same as that used in the low-noise wind tunnel test (see Figure 4), which consisted of three coaches, six bogies, wheel trucks, and windshields.

Validation was performed to ensure the accuracy of the solutions obtained from the simulation mesh with respect to the wind tunnel data. Force coefficients and pressure coefficients are typically used to verify simulations against the results of wind tunnel tests. In this paper, the drag coefficient C_d, the lift coefficient C_l, and the mean static pressure coefficient C_p are defined as follow:

$$C_d = \frac{F_d}{(1/2)\,\rho A u^2},$$
$$C_l = \frac{F_l}{(1/2)\,\rho A u^2}, \quad (5)$$
$$C_p = \frac{p - p_0}{(1/2)\,\rho u^2},$$

where F_d is the time-averaged drag force; F_l is the time-averaged lift force; A is the reference area, $A = 0.186\,\text{m}^2$; p_0 is the atmospheric pressure, $p_0 = 1$ atm; and u is the wind speed, $u = 55.5556$ m/s (200 km/h).

The time-averaged drag and lift coefficients obtained from the DES calculations are listed in Table 4 (for a wind speed of 200 km/h). Figure 7 shows a comparison of the pressure coefficients at electronic pressure scanners P1 and P2 from the numerical simulation and the wind tunnel test. As Table 4 shows, little difference in the results is evident between the simulation and the wind tunnel. The differences in the drag coefficients between the simulated and experimental results are within 2.07%, and the differences in the lift coefficients are within 8.33%. This discrepancy is believed to be attributable to the difference in the ground simulation between the CFD calculations and the wind tunnel. Figure 7(a) shows that the maximum pressure throughout the entire train is located at the nose of the head train and that this maximum value is 1909 Pa, corresponding to a stagnation pressure coefficient of approximately 1.01. Moreover, Figures 7(b) and 7(c) also show that the computational results are very close to the wind tunnel test results; the error on the pressure coefficients is approximately 0.9%, which is sufficient to satisfy the accuracy requirements for engineering application. Thus, the proposed numerical simulation method is reliable and valid for assessing the aerodynamic performance of low-noise design schemes.

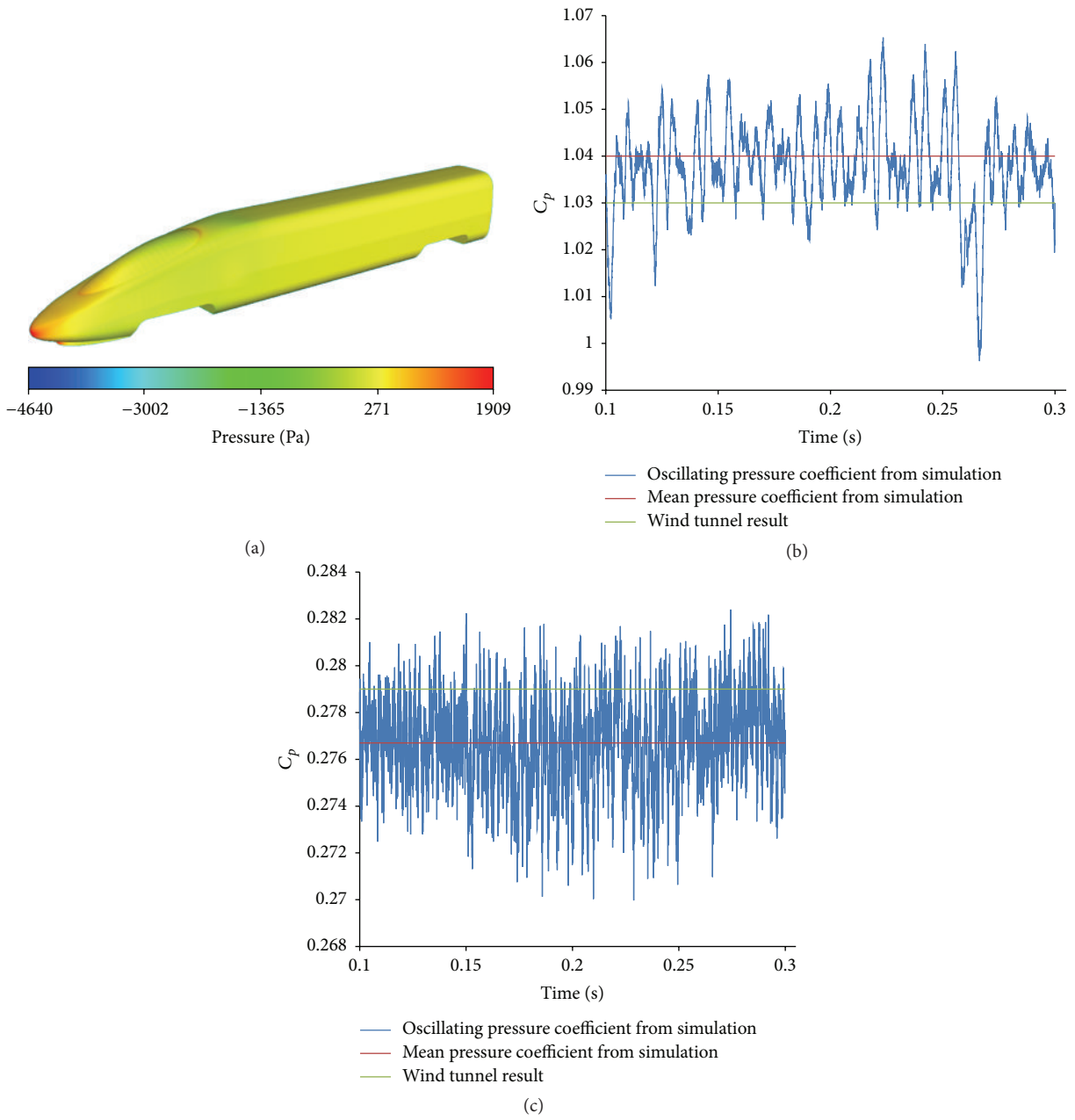

FIGURE 7: Comparison of pressures and pressure coefficients: (a) simulated pressure distribution on the head train, (b) pressure coefficient at P1, and (c) pressure coefficient at P2.

5. Characteristics of the Aerodynamic Noise of High-Speed Trains

5.1. Characteristics of the Flow Structures. The main noise sources for high-speed trains are predominantly dipole sources [1, 4], and the dipole sources on train surfaces are determined by pressure fluctuations on the train surface. The sizes of these sources reflect the near-field radiation of the sound from the surface. As an indicator of turbulence, the turbulence kinetic energy (TKE), which is expressed as $k = (1/2)(\overline{u'}^2 + \overline{v'}^2 + \overline{w'}^2)$, can be used to evaluate the noise distribution along the train surface [14, 35].

The surface TKE distribution in the pantograph fairing region is shown in Figure 8. Substantial TKE is distributed at the points of transition between the leading edge of the pantograph fairing and the folded pantograph, the fairing region, and the second inter-coach spacing. The turbulence from the front of the pantograph fairing surges on the folded pantograph, resulting in near-field noise. Noise radiation in the region of the lifted pantograph is enhanced by impinging turbulence and vortex shedding. The second inter-coach spacing, also with high TKE, is also considered to be a major noise source.

The flow field represented by the isosurface of the normalized second invariant of the velocity gradient, as indicated

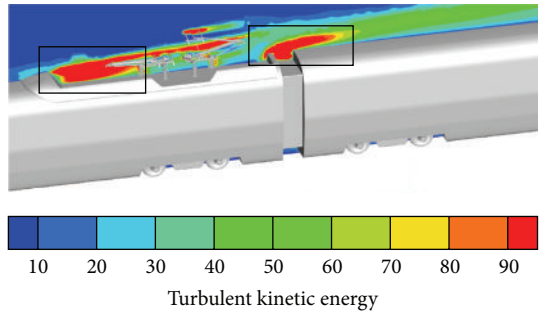

Figure 8: TKE distribution in the pantograph fairing region.

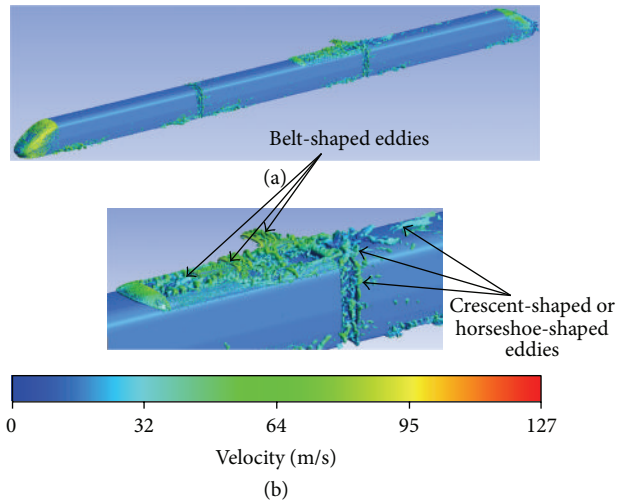

Figure 9: Isosurface of the instantaneous normalized Q-criterion ((a): entire vehicle; (b): magnified view).

by the Q-criterion (at a level of 0.00253) and coloured according to the velocity magnitude, is displayed in Figure 9. This figure shows that the flow around the pantograph region is characterized by considerable coherent alternating shedding of vortices with different sizes and orientations. More specifically, the airflow first reaches the leading edge of the pantograph recess, where belt-shaped eddies form. Then, these eddies impinge on the first pantograph, and the vortices substantially deform and separate. Some eddies enter the cavity of the pantograph recess and decrease in velocity, some impinge on the second pantograph and again form belt-shaped eddies, and the remaining eddies are reshaped into crescent-shaped or horseshoe-shaped eddies in the second inter-coach spacing. These remaining eddies move farther downstream along the coach, alternatively detaching from and reattaching to the train surface. Vortex shedding is observed at the train head, the first bogie region, the first inter-coach spacing, the pantograph region (including the pantographs), the second inter-coach spacing, the train tail, and other bogies, all of which together may represent the main aerodynamic noise sources for high-speed trains.

5.2. Aerodynamic Noise Source. In many engineering applications concerns, turbulence poses broadband noise problems; that is, there is no obvious dominant frequency band and the wide-band range of noise or sound energy presents a continuous frequency distribution. Radiated aerodynamic noise is a typical type of broadband noise, which exhibits a frequency spectrum covering a wide range of frequencies. The Proudman equation [36] is widely applied to describe such noise. Proudman used Lighthill's acoustic analogue theory and ignored the delay differential, which he replaced with the effective synchronous covariance, to deduce the expression for the sound power radiated per unit volume of isotropic turbulence at low M and a high Reynolds number. Recently, Lilley [37] reconsidered adopting a delay differential to deduce an expression for the radiated sound power. The expression for the radiated sound power P_A (expressed in W/m^3) per unit volume of isotropic turbulence can be derived as follows based on both of these approaches:

$$P_A = \alpha\rho\left(\frac{u^3}{l}\right)\frac{u^5}{c_0^5}, \tag{6}$$

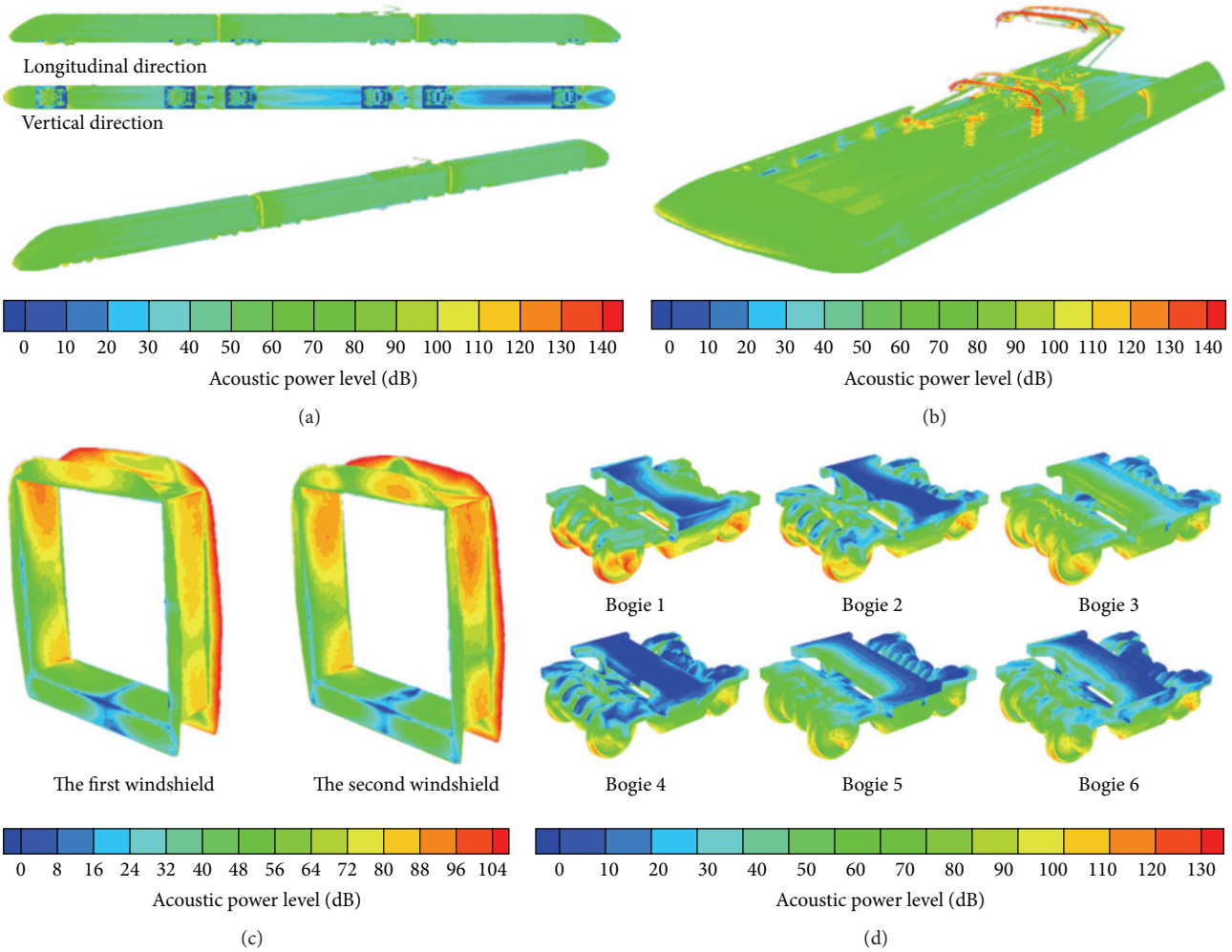

FIGURE 10: Sound power contours for the high-speed train: (a) the entire vehicle, (b) the pantograph fairing region, (c) the inter-coach spacings, and (d) the bogies.

where u is the turbulence velocity, l is the length scale of the turbulence, and α is a numerical constant. Using the TKE k and the turbulence dissipation rate ε, (6) can be rewritten as

$$P_A = a_\varepsilon \rho_0 \varepsilon M^5, \tag{7}$$

where

$$M = \frac{\sqrt{2k}}{c_0}. \tag{8}$$

Sarkar and Hussaini [38] used DNS to compute the isotropic turbulence and obtained $\alpha_\varepsilon = 0.1$. For turbulence in a specific region, the Proudman equation can be used to calculate the sound power per unit volume if the flow is characterized by a high Reynolds number, a low M, and isotropic turbulence. Sound power [31] is defined as

$$L_w = 10\lg\frac{P_A}{P_r}, \tag{9}$$

where P_r is the reference sound power and $P_r = 10^{-12}\ \mathrm{W/m^3}$.

In the numerical simulations, the RNG k-ε turbulence model was first applied to simulate the steady and transient flow fields around the high-speed train considered in this study and to extract k and ε for each node in the transient flow field. Second, the sound power per unit volume at each node was calculated using the Proudman equation to obtain the distribution pattern of the sound power over the surface of the high-speed train.

The L_w distribution contours for the entire vehicle, the pantograph region, the inter-coach spacings, and the bogies are shown in Figure 10. The peak value of L_w is greater than 100 dB at, for example, the power head nose, the head cowcatcher, the head windscreen wiper, the bogies, the pantographs, the pantograph fairing region, the inter-coach spacing, the tail windscreen wiper, and the windward-side area of the first bogie. The L_w values the bluff bodies of the head and tail trains are smaller. The aerodynamic noise increases with increasing fluctuating pressure at locations where L_w is higher on the train surface.

The L_w values on the windward side of the pantograph, including the panhead, base frame, balance rod, pneumatic

pantograph lifting device, and insulators, exceed 110 dB, as shown in Figure 10(b). The maximum L_w values at the base frame, panhead, and insulators are 139.9, 137.8, and 128.9 dB, respectively, when the first pantograph is folded. By contrast, when the second pantograph is in the usage state, the maximum L_w values at the panhead, base frame, balance rod, pneumatic pantograph lifting device, and insulators are 140.4, 128.1, 126.9, 120.4, and 119.9 dB, respectively. Therefore, the most important pantograph noise sources are the convex locations on the windward side. Significant noise reduction can be achieved if the panhead and base frame are shaped with streamlined bodies.

Because the pantograph region (including the pantograph fairing) significantly affects the disturbance of the airflow at the second inter-coach spacing, both the sound power and the noise distribution range at the second inter-coach spacing are larger than those at the first inter-coach spacing, as illustrated in Figure 10(c). Therefore, the main aerodynamic noise sources are distributed in areas where the change in part curvature is severe or the vortices are strong (see Figure 9).

Moreover, the maximum L_w values at the first bogie on the head train is larger than those at the other bogies, and the L_w distribution is broader. For example, the maximum L_w values at the first and second bogies on the head train are 123.8 and 108.1 dB, respectively, whereas the maximum L_w values at the first and second bogies on the mid train are 101.1 and 92.0 dB, respectively. Similarly, on the tail train, the maximum L_w values at the first and second bogies are 91.6 and 89.1 dB, respectively.

Thus, the main noise sources on a high-speed train are the pantographs, the head windscreen wiper, the bogies, the pantograph fairing region, the head cowcatcher, the windward-side areas of bogie regions, the inter-coach spacing, and the power head nose. The noise sources on a high-speed train are located where the airflow is easily separated and where turbulent motion is strong.

5.3. Characteristics of Far-Field Aerodynamic Noise

5.3.1. SPL Distribution Characteristics. According to the ISO3095-2013 standard, far-field noise evaluation points were defined in this study that were located 25 m away from the centre line of the track and 3.5 m above the ground on one side of the train. Along the axis of the train, starting from the head nose and proceeding to the tail nose, far-field noise evaluation points were defined every 1 m. Consequently, 82 noise evaluation points were defined in total. All noise evaluation points were tested under the same conditions unless otherwise stated.

The $L_{pAeq,T}$ values at the evaluation points along the train are shown in Figure 11. From the head nose to $x = 5$ m, the SPL rapidly increases by 11.6 dB(A). The SPL reaches its global maximum of 91.2 dB(A) at $x = 5$ m, beyond which the SPL gradually decreases along the remaining length of the train up to streamlined taper to the tail, where the SPL rapidly decreases by 12.2 dB(A). In addition, the SPL exhibits local maxima at the second bogie of the head train, the first and second bogies of the mid train, and the first and second bogies

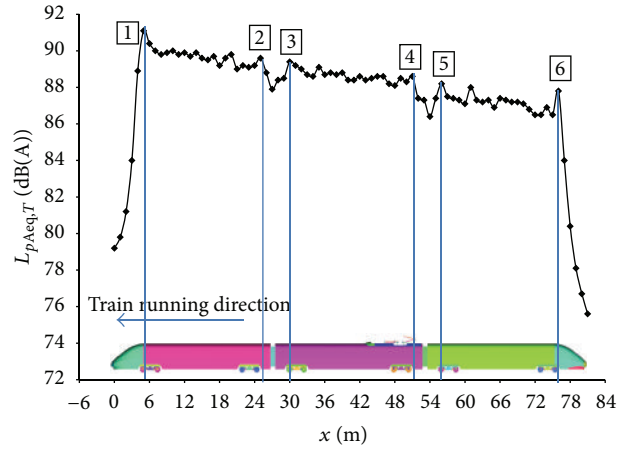

Figure 11: SPL distribution along the high-speed train.

of the tail train. Thus, for the noise evaluation points along the high-speed train, $L_{\max}$ of 91.2 dB(A) and L_{pm} of 88.5 dB(A) were obtained through simulation.

Figure 11 also shows that the SPL values are lower in the inter-coach spacing region between 2 and 3 (and similarly between positions 4 and 5). This is because the sound propagation in this region appears to be divided into two components. One component is generated from self-sustained oscillation [39] in the inter-coach cavity and propagates upstream, whereas the other is induced by aerodynamic pressure fluctuation on the train surface and spreads downstream. Finally, the noise radiation from the inter-coach spacing region manifests in two branches: one originating from the cavity and extending along the upstream side of the inter-coach spacing and one originating from the surface of the train and extending in the downstream direction. Therefore, the SPL values at the noise points within an inter-coach spacing region are smaller than those on either side (upstream and downstream).

5.3.2. Spectra Characteristics. The power spectral density (PSD) of a short-record signal in time can be determined using Welch's method. The signal processing approach used in [24], in which the signal is separated into six segments, each with 50% overlap, was followed in this study. A Hanning window was applied to each segment, and the PSDs for all segments were averaged and compensated. Compared with the complete analysis of the entire signal, this method offers the advantage of reducing the variance of spectral estimates for short records in time.

The sound pressure spectrum at noise evaluation point $x5$ (the noise evaluation point corresponding to the longitudinal maximum SPL) is shown in Figure 12. This figure illustrates that the aerodynamic noise spectrum of the high-speed train extends over a wide frequency domain and can be considered broadband noise, with the main energy-containing frequencies concentrated between 800 and 4000 Hz. It must be mentioned that the Doppler effect introduced by the train pass-by is not taken into account in the spectra presented in Figure 12. A direct comparison with a measured spectrum during train pass-by is not coherent [4, 15].

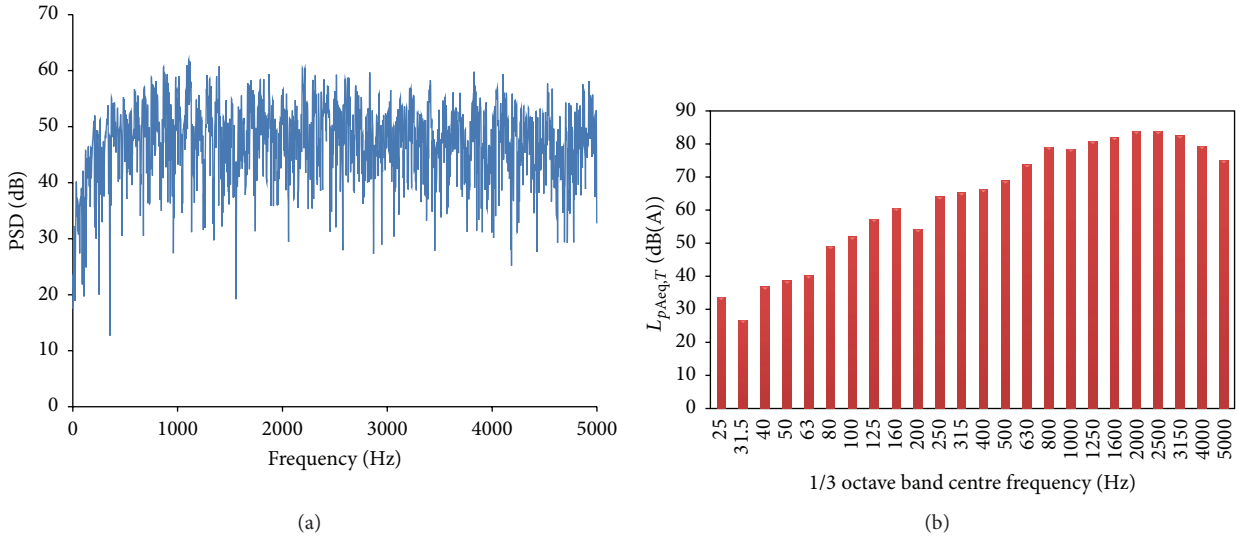

Figure 12: Sound pressure spectrum at $x5$.

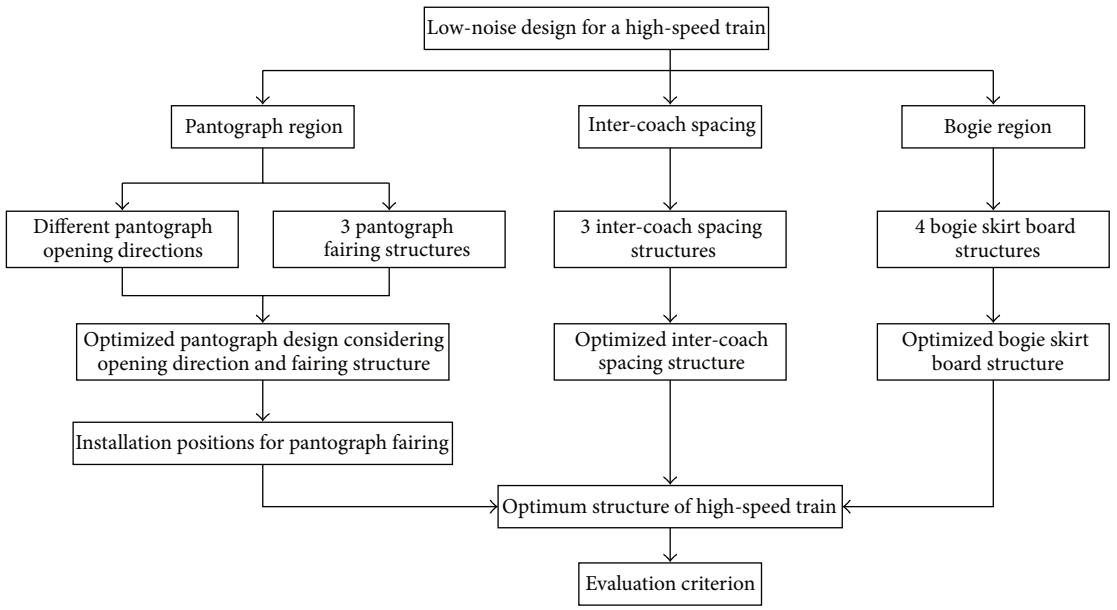

Figure 13: Flow chart of the low-noise design process for a high-speed train.

6. Noise Reduction Analysis Based on the Main Noise Sources

The main noise sources were determined using the Proudman equation as described above. Optimizing the structures of the main noise sources can lead to effective noise reduction. The main structural aspects considered for such optimization in this work are as follows: two different operation orientations of the pantographs, three different structures of the pantograph fairing, two different installation positions of the pantograph fairing, different pantograph lifting configurations, three different structures of the inter-coach spacings, and four different structures of the bogie skirt boards. The low-noise design process for a high-speed train is detailed in Figure 13.

6.1. Mitigation of Pantograph-Region Noise

6.1.1. Different Operation Orientations of the Pantographs. To investigate the influence of the operation orientation of a pantograph on the associated aerodynamic noise, a computational region was established as shown in Figure 14. The physical model is a simplified version of the real geometric structure of the DSA380 high-speed pantograph. The DSA380 pantograph is a single-arm pantograph used on CRH380B high-speed trains in China. The dimensions of the pantograph are approximately $L = 2.44$ m, $H = 1.63$ m, and $W = 2.02$ m in the x-, y-, and z-directions, respectively. The computational domain has dimensions of $25L \times 6H \times 12W$. The pantograph is placed at the centre of the domain in

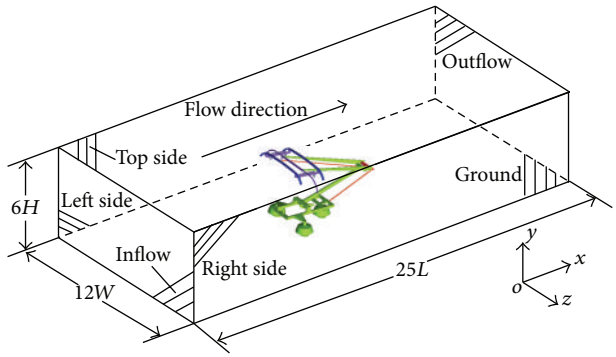

FIGURE 14: Schematic diagram of the computational domain for the pantograph model.

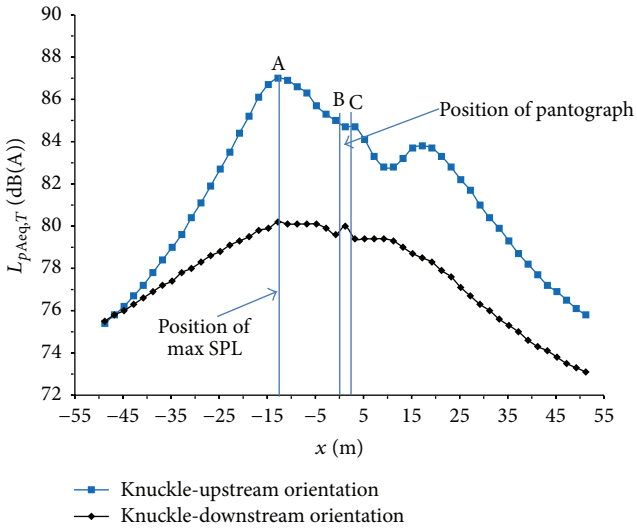

FIGURE 15: Comparison of the longitudinal SPL distribution for the two operation orientations.

both the x- and z-directions, and the distance between the insulators and the ground is 0.376 m.

The single-arm pantograph model was tested in two operation orientations: the knuckle-upstream orientation and the knuckle-downstream orientation. When the pantograph is raised to touch the contact wire in the knuckle-downstream orientation, as shown in Figure 14, the incoming flow is in the positive x-direction. Conversely, when the pantograph is placed in the knuckle-upstream orientation, the incoming flow is from the negative x-direction.

A diagram comparing the longitudinal SPL distributions for the two opening orientations of the pantograph at a running speed of 350 km/h is shown in Figure 15. The positions of the noise evaluation points are set 16 m from the centre of the pantograph and 1.2 m above the ground. The SPL values for the knuckle-downstream orientation are smaller than those for the knuckle-upstream orientation; the discrepancies between the $L_{\max}$ and L_{pm} values in the two cases are 7.1 dB(A) and 3.9 dB(A), respectively. In the knuckle-upstream orientation, the pantograph is significantly affected by the wake flow; thus, $L_{\max}$ is 87.3 dB(A) at $x = -12.78$ m.

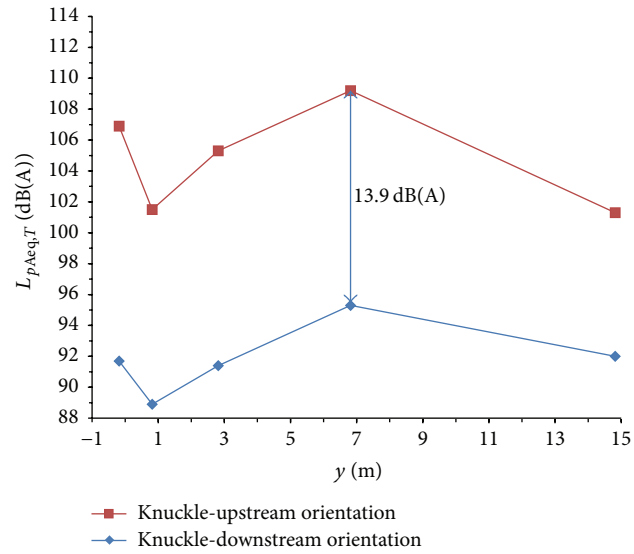

FIGURE 16: Comparison of the SPL values at vertical evaluation points for the two pantograph opening orientations.

TABLE 5: The coordinates of each noise evaluation point.

Point site	b1	b2	b3	b4	b5
x-coordinate/m	1.22	1.22	1.22	1.22	1.22
y-coordinate/m	−0.18	0.82	2.82	6.82	14.82
z-coordinate/m	4	4	4	4	4

The turbulent flow has less influence on the pantograph in the knuckle-downstream orientation; in this case, $L_{\max}$ is only 80.2 dB(A) at $x = -12.78$ m.

Similarly, a comparison of the vertical SPL distributions is presented in Figure 16. The positions of the noise evaluation points are listed in Table 5. The five selected measuring points are labelled b1–b5. The distance between each pair of adjacent measuring points is twice that between the previous pair. At a height of 7.19 m above the ground (b4), the SPL reaches its maximum value. The maximum value of the knuckle-downstream orientation is 13.9 dB(A) lower than that for the knuckle-upstream orientation.

Measuring point b4, where the SPL reaches its maximum, was chosen as the object of further analysis. Comparisons of the PSDs and the 1/3 octave band spectra for the two pantograph orientations are presented in Figure 17. The results shown in Figure 17(a) indicate that when the pantograph is operating in either orientation, the dominant frequencies are 305, 608, and 913 Hz, and the corresponding SPLs in the knuckle-downstream orientation are 11.3, 6.5, and 2.2 dB lower than those in the knuckle-upstream orientation. Figure 17(b) shows that when the pantograph is operating in either orientation, the far-field aerodynamic noise energy is concentrated in the range of 250 to 1000 Hz and peaks at central frequencies of 315 Hz and 630 Hz, where the corresponding SPLs in the knuckle-downstream orientation are lower 9.1 dB(A) and 6.7 dB(A), respectively, than those in the knuckle-upstream orientation.

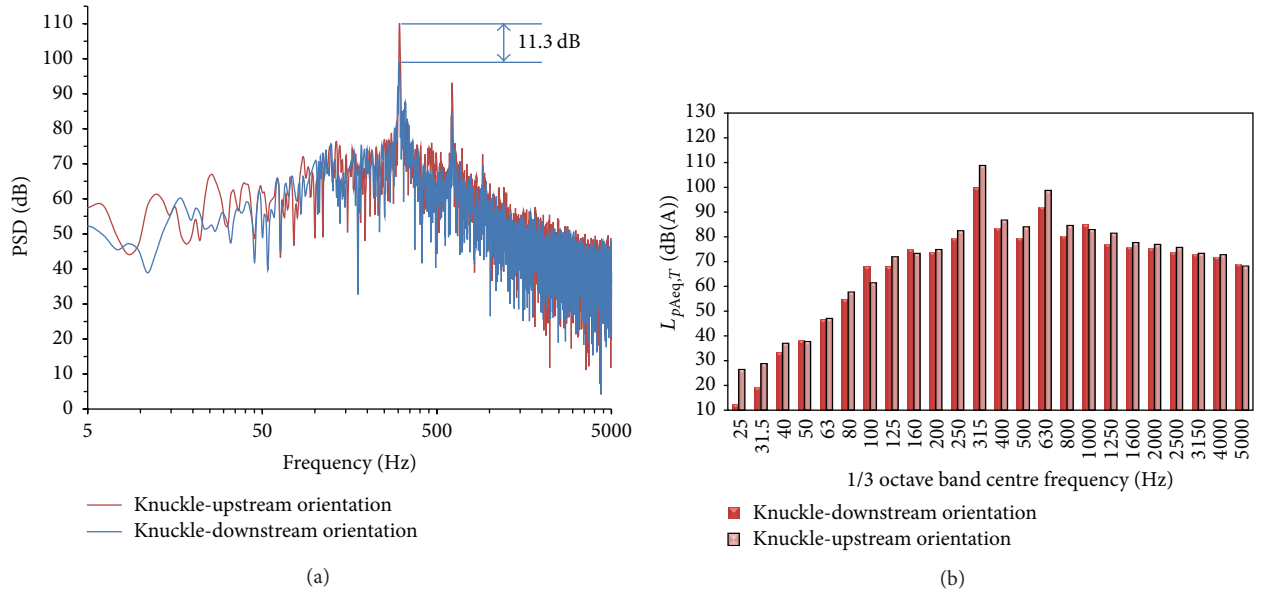

Figure 17: Spectral comparisons at b4: (a) PSDs and (b) 1/3 octave band centre frequencies.

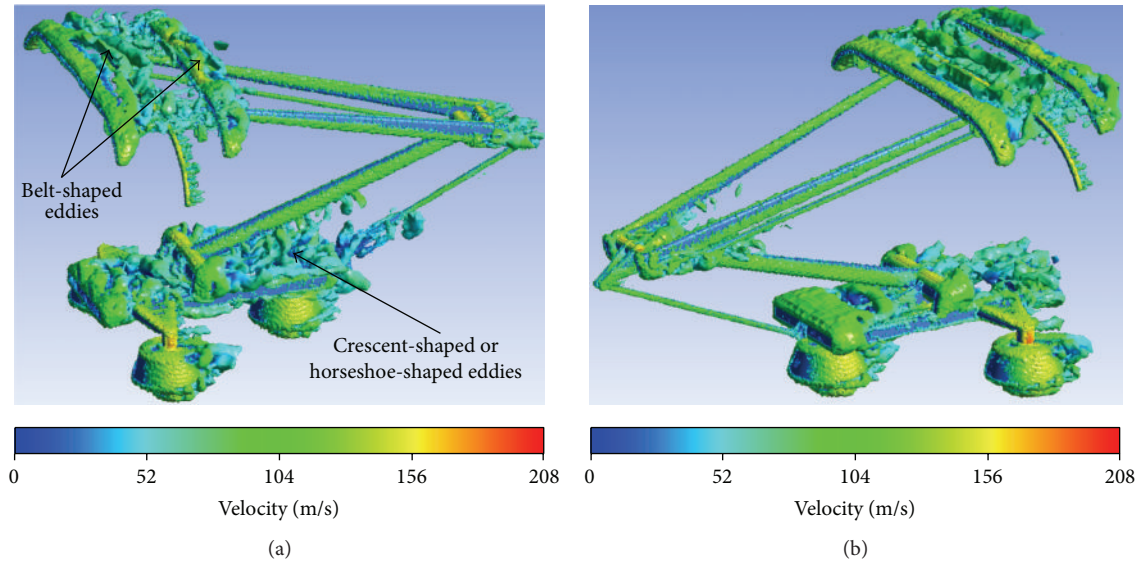

Figure 18: Isosurfaces of the instantaneous normalized Q-criterion: (a) the knuckle-downstream orientation and (b) the knuckle-upstream orientation.

Figure 18 shows the flow field as represented by the isosurface of the normalized second invariant of the velocity gradient indicated by the Q-criterion (at a level of 0.00253) and coloured according to the velocity magnitude (the pantograph speed is 350 km/h). The flow around the pantograph is characterized by considerable coherent alternating shedding of vortices with varying sizes and orientations. More specifically, the airflow first reaches the leading edge of the panhead, where belt-shaped eddies form, as illustrated in Figure 18. Then, these eddies leave the leading edge of the panhead and are carried by the airflow to the trailing edge of the panhead. Meanwhile, the eddies from the base frame and insulators impinge on the trailing edge of the base frame; these vortices substantially deform and separate. Some eddies enter the cavity of the base frame and decrease in velocity, and the remaining eddies are reshaped into crescent-shaped or horseshoe-shaped eddies. These remaining eddies move farther downstream along the back end of the pantograph while alternately detaching from and reattaching to the structure.

According to the contrast analysis, larger vortices are generated at the pantograph knuckle and the back end of the panhead when the pantograph is in the knuckle-upstream orientation. In addition, vortex shedding and reconstruction more negatively influence the flow field than they do in the knuckle-downstream orientation.

(a) (b)

Figure 19: Two different pantograph fairing structures: (a) Dlz2 and (b) Dlz3.

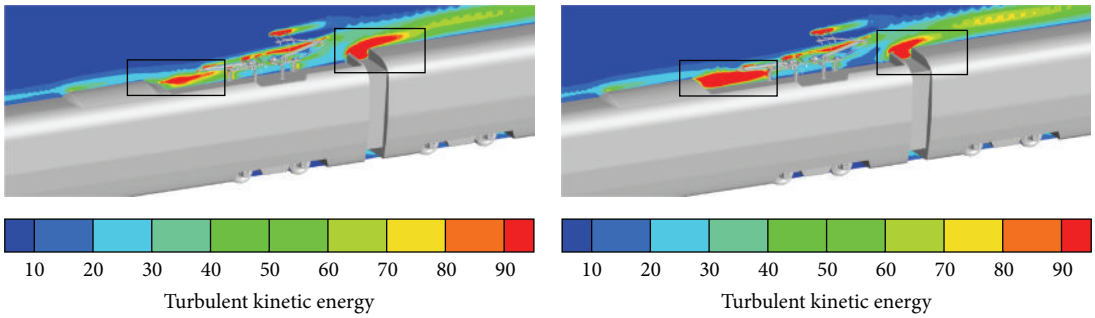

(a) (b)

Figure 20: TKE distributions in the pantograph fairing regions: (a) Dlz2 and (b) Dlz3.

According to the above analysis of the far-field aerodynamic noise induced by a pantograph, the knuckle-downstream pantograph orientation should be chosen to improve aerodynamic performance and reduce noise.

6.1.2. Effect of the Pantograph Fairing Design. Two different types of pantograph fairings are presented in Figure 19: Dlz2 and Dlz3. In the Dlz2 type, the air-conditioning unit structure is separated from the pantograph fairing, whereas, in the Dlz3 type, the air-conditioning unit structure is connected to the pantograph fairing.

The TKE distributions for the different pantograph fairing regions are shown in Figure 20. Compared with Dlz1 (see Figure 8), the high-TKE zones of both Dlz2 and Dlz3 are reduced, especially between the air-conditioning unit and the first pantograph. In addition, the TKE values at the second pantograph and the inter-coach spacing are also reduced. A comparison of the TKE distributions for the different pantograph fairing structures reveals that both the flow-field distribution and the near-field aerodynamic performance of Dlz2 are superior to those of Dlz3.

Figure 21 compares the longitudinal SPL distributions of the two different pantograph fairing structures at 82 noise evaluation points. Based on the analysis presented in Figure 21 and Table 6, $L_{\max}$ for Dlz2 is 0.4 dB(A) lower than that for Dlz3 and 0.7 dB(A) lower than that for Dlz1. L_{pm} for Dlz2 is 0.4 dB(A) lower than that for Dlz3 and 0.6 dB(A) lower than that for Dlz1.

Figure 22 shows the constant vortex diagrams based on the Q-criterion (at a level of 0.00253) for the different pantograph fairing structures. For Dlz3, a large vortex is created by the air-conditioning unit and the folded pantograph area, which aggravates vortex shedding and reconstruction. For Dlz2, a stepped structure appears between the air-conditioning unit and the pantograph fairing region, which cushions the vortex shedding of the air-conditioning

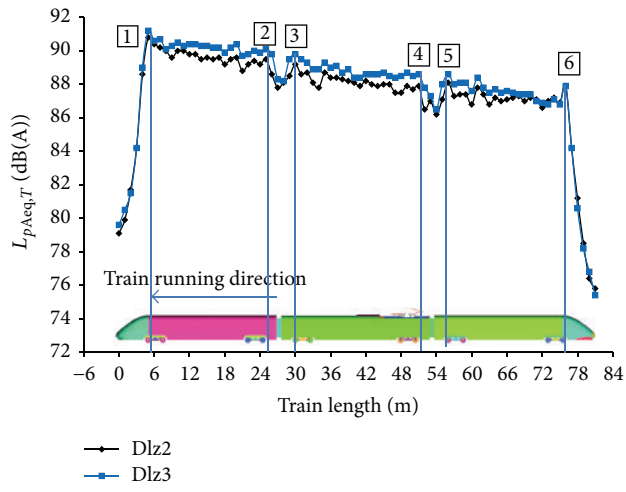

Figure 21: Comparison of the longitudinal SPL distributions for two different pantograph fairing structures.

Table 6: Comparison of the SPL indices for the different pantograph fairing structures (dB(A)).

Evaluation index	Dlz1	Dlz2	Dlz3
$L_{\max}$	91.2	**90.5**	90.9
L_{pm}	88.5	**87.9**	88.3

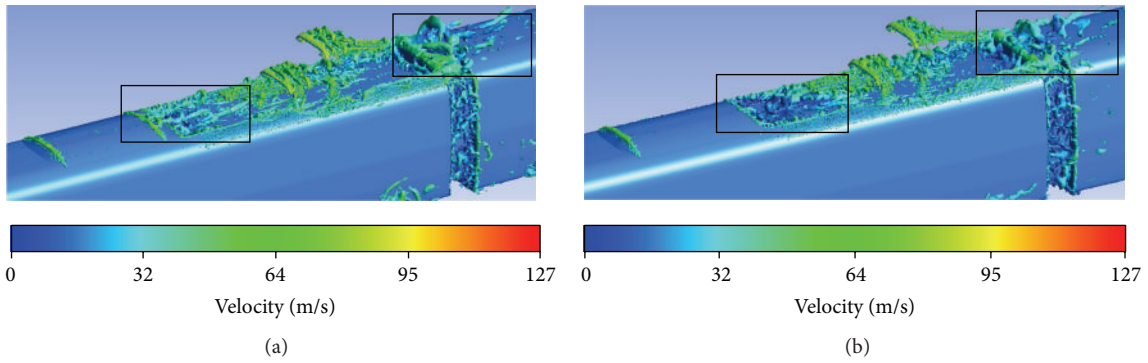

Figure 22: Isosurfaces of the instantaneous normalized Q-criterion for different pantograph fairing structures: (a) Dlz2 and (b) Dlz3.

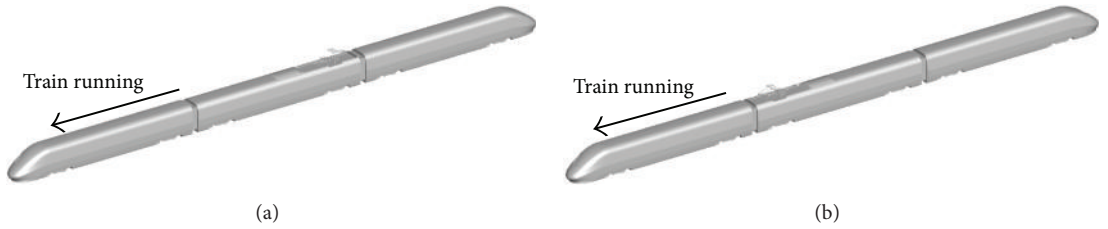

Figure 23: Different pantograph fairing installation positions: (a) rearward position and (b) forward position.

unit against the folded pantograph. Thus, a smaller vortex forms that has little influence on the flow-field structures in the pantograph fairing region. A larger vortex arises near the pantograph fairing and in the second inter-coach spacing. However, the vortex formed in the case of Dlz3 is larger and wider than that in the case of Dlz2. Therefore, the flow-field performance of Dlz2 is superior to that of Dlz3; consequently, the noise reduction effect of Dlz2 is also superior and this structure should be adopted to improve aerodynamic performance and reduce noise.

6.1.3. Different Pantograph Fairing Installation Positions. The aerodynamic noise characteristics for a pantograph fairing installed near the second inter-coach spacing are analysed above (see Figure 22(a)). This section focuses on aerodynamic performance and characteristics of a pantograph fairing installed near the first inter-coach spacing. Figure 23 shows the calculation models used in this section for both the rearward and forward positions of the pantograph fairing.

Figure 24 shows the TKE distribution for the high-speed train travelling in the reverse direction (equivalent to shifting the placement of the pantograph fairing from the rearward to the forward position). Compared with the rearward position of the pantograph fairing, the forward position results in stronger and wider TKE distribution between the first inter-coach spacing and the lifted pantograph as well as a stronger TKE in the insulator region. Therefore, when the high-speed train runs in the reverse direction, the noise radiated from this aerodynamic noise source may be much stronger.

Figure 25 compares the longitudinal SPL distributions for the different installation positions of the pantograph fairing with respect to the train's direction of travel. As seen in

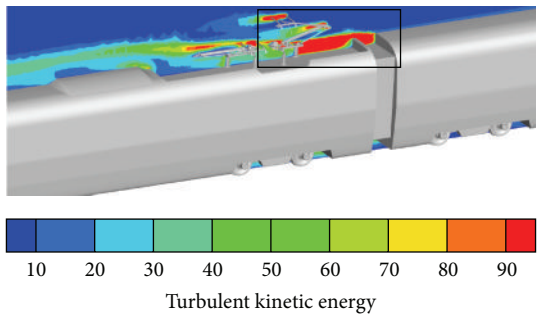

Figure 24: TKE distribution of the pantograph fairing region with the train running in the reverse direction.

Figure 25, the $L_{\max}$ value for the forward position of the fairing is 93.6 dB(A), and L_{pm} is 90.4 dB(A). Compared with the SPL indices for the fairing in the rearward position, these $L_{\max}$ and L_{pm} values are 3.1 dB(A) and 2.5 dB(A) higher, respectively. These results indicate that, in terms of reducing aerodynamic noise, the installation of the pantograph fairing near the second inter-coach spacing is more appropriate.

6.1.4. Different Pantograph Lifting Configurations. This section focuses on the effect on the aerodynamic noise exerted by the choice of which pantograph is lifted in the double pantograph. The geometric models are presented in Figure 26. The two pantographs, the pantograph fairing, and the two air-conditioning units are installed on the mid train at the central position to reduce the influence of the inter-coach spacings on the aeroacoustic behavior and noise associated with the different lifted-pantograph positions. A pair of air-conditioning units is also placed in the centre of

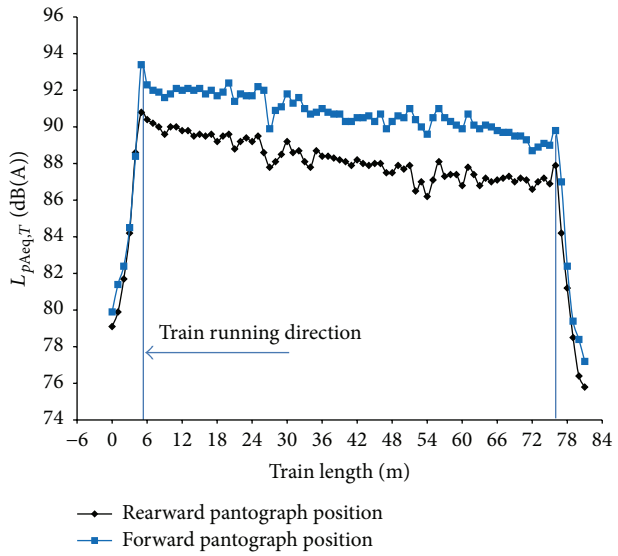

Figure 25: Comparison of the longitudinal SPL distributions for different pantograph fairing installation positions.

Figure 26: The geometric models of the lifting of different pantographs: (a) Sg1 and (b) Sg2.

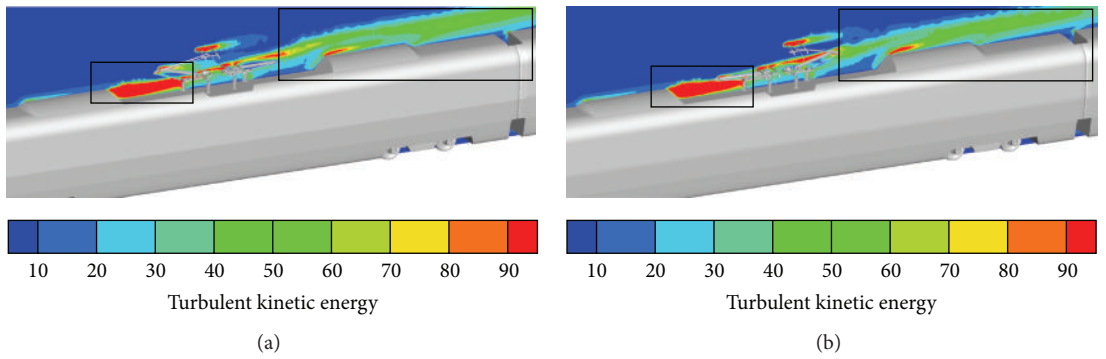

Figure 27: TKE distributions for different pantograph lifting configurations ((a): Sg1; (b): Sg2).

the pantograph fairing. In the configuration denoted by Sg1, the first pantograph is lifted and the second pantograph is folded, as shown in Figure 26(a). Conversely, in configuration Sg2, shown in Figure 26(b) the first pantograph is folded and the second pantograph is lifted.

Figure 27 shows the TKE distributions around the pantographs in the different lifting configurations. Sg1 results in stronger and wider TKE distributions at the air-conditioning unit, the leading edge of the fairing, and the back of the second pantograph. Compared with Sg2, the TKE near the lifted pantograph also presents a stronger and wider distribution. Therefore, the noise radiation induced by Sg2 is much weaker.

Figure 28 compares the longitudinal SPL distributions for high-speed trains with different pantograph lifting configurations. According to Figure 28, the $L_{\max}$ and L_{pm} values for Sg1 are 90.2 dB(A) and 86.9 dB(A), whereas those for Sg2 are 89.9 dB(A) and 86.6 dB(A), respectively. Compared with the SPL indices for Sg1, these values are lower by 0.3 dB(A) and 0.3 dB(A), respectively. Therefore, it can be concluded

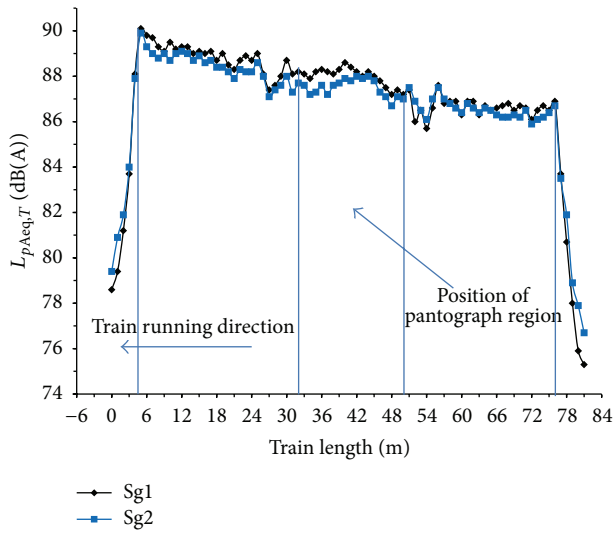

Figure 28: Comparison of the longitudinal SPL distributions for different pantograph lifting configurations on a high-speed train.

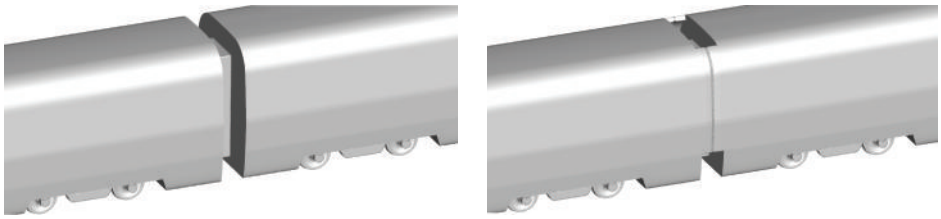

Figure 29: The geometric models of two types of inter-coach spacings: (a) Fd2 and (b) Fd3.

that lifting the second pantograph is preferable for reducing aerodynamic noise.

6.2. Low-Noise Design for Inter-Coach Spacings. An inter-coach spacing in a train is a cavity with a particular streamwise length/depth (L/D) ratio. The flow physics can differ for different L/D ratios. The region defined by top, sides, and bottom of the inter-coach spacing acts aerodynamically as an "open" cavity [1, 4, 19], and the aerodynamic noise generation mechanism in this region can be characterized as self-sustained oscillation [40]. Specifically, a highly unsteady shear layer detaches from the leading edge of the top and sides of the inter-coach spacing and impinges on the trailing edge. Thus, a large recirculating flow forms in the cavity, and acoustic pressure propagates upstream, which strengthens the unsteadiness of the upstream shear layer [41]. Thus, it is essential to reduce inter-coach spacing noise.

Two types of inter-coach spacing, labelled Fd2 and Fd3, are illustrated in Figure 29. The dimensions of Fd2 are L = 6.36 m, W = 1.25 m, and H = 2.91 m. To obtain the structure of Fd3, two diaphragm plates are added to Fd2 on both sides of the inter-coach cavity to form a semienclosed diaphragm plate structure.

Figure 30 compares the TKE distributions induced by these two designs in the second inter-coach spacing area, which is the inter-coach spacing area with the stronger TKE and thus is considered to be the main noise source. For Fd3, the TKE in this inter-coach spacing area is more evenly distributed and weaker than that for Fd2, especially on the windward side of the inter-coach spacing. Thus, the noise power and radiated noise in the case of Fd2 are higher and exhibit greater turbulence.

Figure 31 compares the longitudinal SPL distributions for high-speed trains with different inter-coach spacing designs. According to Figure 31, the $L_{\max}$ and L_{pm} values for Fd3 are 89.7 dB(A) and 87.7 dB(A), respectively. This $L_{\max}$ is 0.4 dB(A) lower than that for Fd2, and L_{pm} is 0.3 dB(A) lower. These results demonstrate that the aerodynamic performance and noise reduction effects of Fd3 are superior.

6.3. Noise Reduction in the Bogie Regions. The bogies are considered to be the main sources of aerodynamic noise on high-speed trains. However, it is difficult to reduce noise by using streamlined designs for these structures because of their complexity and the turbulent vortices in the flow field. Optimization by means of bogie skirt boards is one of the most common mitigation measures. Bogie skirt boards can serve as sound barriers for sound insulation against near-field noise radiation, thereby also decreasing the far-field noise radiation [42].

Four types of bogie skirt board structures are presented in Figure 32: Qb1, Qb2, Qb3, and Qb4. The Qb1 structure

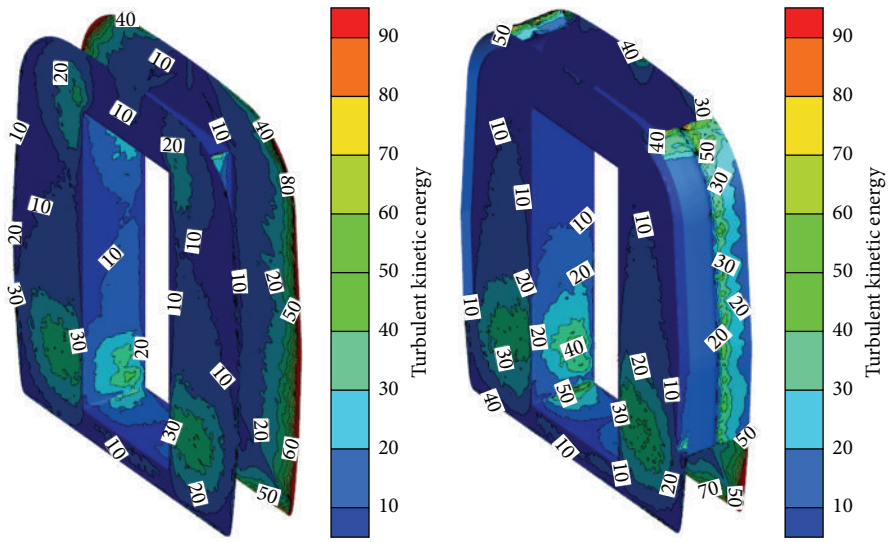

Figure 30: TKE distributions in the second inter-coach spacing: (a) Fd2 and (b) Fd3.

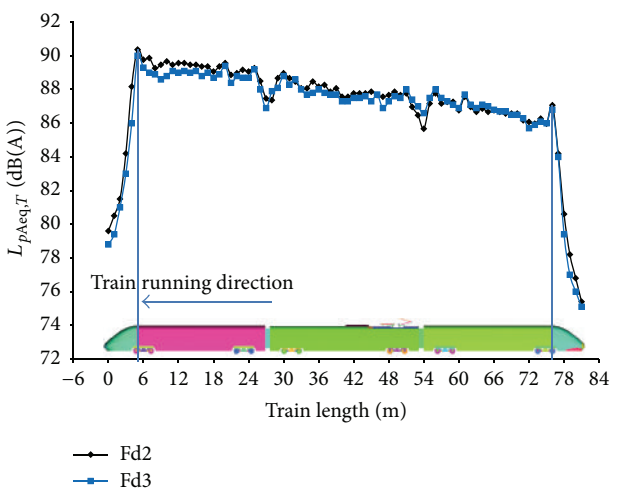

Figure 31: Comparison of the longitudinal SPL distributions for high-speed trains with different inter-coach spacing designs.

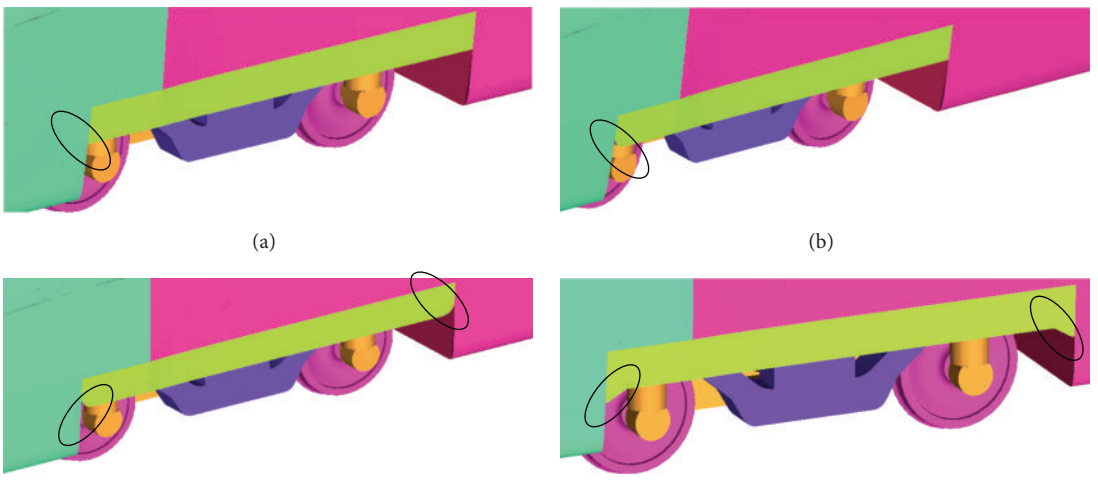

Figure 32: The geometric models of the four bogie skirt board designs: (a) Qb1, (b) Qb2, (c) Qb3, and (d) Qb4.

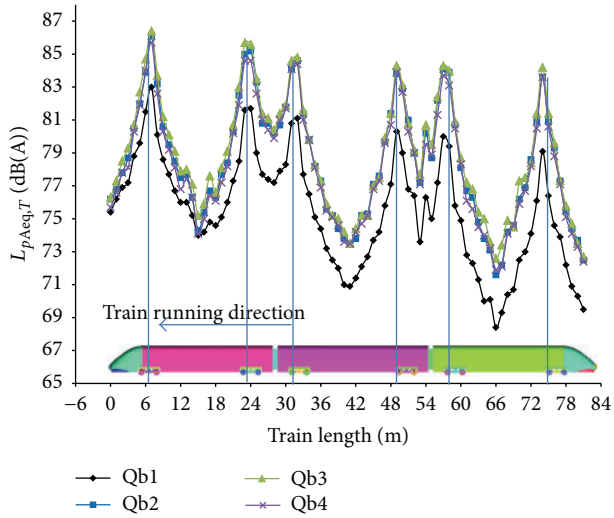

Figure 33: Comparison of the longitudinal SPL distributions for high-speed trains with different bogie skirt board designs.

(a) (b)

Figure 34: The train model after optimization for aerodynamic noise performance: (a) entire vehicle and (b) magnified view.

Table 7: Comparison of the SPL indices for different bogie skirt board designs (dB(A)).

Evaluation index	Qb1	Qb2	Qb3	Qb4
$L_{\max}$	**83.0**	86.1	86.4	85.7
L_{pm}	**76.7**	80.0	80.4	79.7

is the original structure considered in the model, without a rounded corner at the transitional position between the skirt board and the underside of the car body. In Qb2, such a rounded corner is implemented on the leeward side. The Qb3 structure includes rounded corners at both the leeward and windward sides. Finally, the Qb4 structure is obtained by applying a chamfering process at the transitional positions in Qb1.

A comparison of the SPL distributions for high-speed trains with bogies with different bogie skirt board designs, which are selected separately as the main noise sources (including six bogies, the skirt board structures, and the bogie base plates), is shown in Figure 33. The SPL indices $L_{\max}$ and L_{pm} for the different bogie skirt board designs are listed in Table 7. Figure 33 and Table 7 show that the $L_{\max}$ and L_{pm} values for Qb1 are both lower than those for the other bogie skirt board designs. This result indicates that the radiation and propagation of the noise from the bogie are most effectively blocked by bogie skirt boards of the Qb1 type because of the larger longitudinal area of these skirt boards. The results obtained for the four investigated types of skirt boards are as follows: the far-field noise is lowest for Qb1 because the vertical projected area is largest for this design. The $L_{\max}$ values for Qb1 is 3.1 dB(A) lower than that for Qb2, 3.4 dB(A) lower than that for Qb3, and 2.7 dB(A) lower than that for Qb4, and the L_{pm} values for Qb1 is 3.3 dB(A) lower than that for Qb2, 3.7 dB(A) lower than that for Qb3, and 3.0 dB(A) lower than that for Qb4. Thus, compared with the other skirt board structures, the far-field aerodynamic noise performance of Qb1 is substantially superior. The Qb1 structure is recommended for practical engineering applications.

6.4. Optimum High-Speed Train Structure. The optimum geometric high-speed train model for aerodynamic performance and aerodynamic noise is shown in Figure 34. The features of this geometric model are as follows: the second pantograph (toward the rear of the train) is lifted with the pantograph in the knuckle-downstream orientation; the pantograph fairing is mounted on the roof of the mid train and is separated from the air-conditioning unit (Dlz2); a semienclosed inter-coach spacing is used (Fd3); and skirt boards without chamfers or rounded corners are used for all bogies (Qb1). According to the aerodynamic noise calculation and analysis, the $L_{\max}$ and L_{pm} values calculated based on 82 noise evaluation points located 25 m from the centre of the track and 3.5 m above the ground are 3.5 dB(A) and 3.2 dB(A) lower, respectively, than those for the original model.

7. Conclusions

Based on Lighthill's acoustic theory and a broadband noise source model, the DDES and FW-H techniques were used to numerically simulate the aerodynamic noise generated by a high-speed train. The satisfactory accuracy of this calculation method was demonstrated via wind tunnel tests based on scale models. Based on an analysis of the main aerodynamic noise sources and the far-field aerodynamic noise characteristics, strategies for reducing noise by modifying the structures of the main aerodynamic noise sources were recommended.

The main aerodynamic noise sources on a high-speed train are the pantographs, the head windscreen wipers, the bogies, the pantograph fairing, the head cowcatcher, the windward side of the bogie base plate, the inter-coach spacings, and the power head nose. The main noise sources on each pantograph are the panhead, base frame, balance arm, and insulators. The sound power level produced by the first bogie on the head train is higher than those for the other bogies, and the sound power level of the second inter-coach spacing is higher than that of the first.

For current high-speed trains, recommendations for reducing noise are as follows: use the knuckle-downstream pantograph orientation, install the pantograph fairing at the central position on the middle coach, use the knuckle-downstream orientation for the second pantograph when the high-speed train is running in the opposite direction, use the Dlz2 fairing structure (with the air-conditioning units separated from the pantograph fairing), use the Fd3 inter-coach spacing structure (semienclosed with diaphragm plates), and use the Qb1 bogie skirt board structure (with no rounded corners or chamfers at the transitional positions between the skirt boards and train body). These measures have important practical significance for environmental protection and noise reduction for high-speed trains.

A revised low-noise design for a high-speed train was proposed based on the presented numerical analyses. This design will be verified in future studies via on-track tests or wind tunnel experiments. Further work will be needed to deal with the acoustic comfort, especially in the car equipped with the double pantographs at the centre of the middle coach. We suggest also considering the balance between the aerodynamic and the rolling noise in terms of environmental noise reduction.

Competing Interests

The authors declare that there is no conflict of interests.

Acknowledgments

This work was supported by the High-Speed Railway Basic Research Fund Key Project of China (Grant no. U1234208), the National Natural Science Foundation of China (Grants no. 51475394 and no. 51605397), and the Research Project of State Key Laboratory of Traction Power (Grant no. 2016TPL_T02).

References

[1] C. Talotte, "Aerodynamic noise: a critical survey," *Journal of Sound and Vibration*, vol. 231, no. 3, pp. 549–562, 2000.

[2] J. A. Schetz, "Aerodynamics of high-speed trains," *Annual Review of Fluid Mechanics*, vol. 33, pp. 371–414, 2001.

[3] Z.-Y. Shen, "Dynamic environment of high-speed train and its distinguished technology," *Journal of the China Railway Society*, vol. 28, no. 4, pp. 1–5, 2006.

[4] D. J. Thompson, E. Latorre Iglesias, X. Liu, J. Zhu, and Z. Hu, "Recent developments in the prediction and control of aerodynamic noise from high-speed trains," *International Journal of Rail Transportation*, vol. 3, no. 3, pp. 119–150, 2015.

[5] C. Mellet, F. Létourneaux, F. Poisson, and C. Talotte, "High speed train noise emission: latest investigation of the aerodynamic/rolling noise contribution," *Journal of Sound and Vibration*, vol. 293, no. 3–5, pp. 535–546, 2006.

[6] K. Nagakura, "Localization of aerodynamic noise sources of Shinkansen trains," *Journal of Sound and Vibration*, vol. 293, no. 3–5, pp. 547–556, 2006.

[7] T. Kitagawa and K. Nagakura, "Aerodynamic noise generated by Shinkansen cars," *Journal of Sound and Vibration*, vol. 231, no. 3, pp. 913–924, 2000.

[8] W. F. King III, "A précis of developments in the aeroacoustics of fast trains," *Journal of Sound and Vibration*, vol. 193, no. 1, pp. 349–358, 1996.

[9] C. Noger, J. C. Patrat, J. Peube, and J. L. Peube, "Aeroacoustical study of the TGV pantograph recess," *Journal of Sound and Vibration*, vol. 231, no. 3, pp. 563–575, 2000.

[10] T. Sueki, M. Ikeda, and T. Takaishi, "Aerodynamic noise reduction using porous materials and their application to high-speed pantographs," *Quarterly Report of RTRI*, vol. 50, no. 1, pp. 26–31, 2009.

[11] J. Lee and W. Cho, "Prediction of low-speed aerodynamic load and aeroacoustic noise around simplified panhead section model," *Proceedings of the Institution of Mechanical Engineers Part F: Journal of Rail and Rapid Transit*, vol. 222, no. 4, pp. 423–431, 2008.

[12] M. Ikeda, M. Suzuki, and K. Yoshida, "Study on optimization of panhead shape possessing low noise and stable aerodynamic characteristics," *Quarterly Report of RTRI*, vol. 47, no. 2, pp. 72–77, 2006.

[13] T. Kurita, "Development of external-noise reduction technologies for Shinkansen high-speed trains," *Journal of Environment and Engineering*, vol. 6, no. 4, pp. 805–819, 2011.

[14] H.-H. Yu, J.-C. Li, and H.-Q. Zhang, "On aerodynamic noises radiated by the pantograph system of high-speed trains," *Acta Mechanica Sinica*, vol. 29, no. 3, pp. 399–410, 2013.

[15] Y. Wakabayashi, T. Kurita, H. Yamada, and M. Horiuchi, "Noise measurement results of shinkansen high-speed test train (FASTECH360S,Z)," in *Noise and Vibration Mitigation for Rail Transportation Systems: Proceedings of the 9th International Workshop on Railway Noise, Munich, Germany, 4–8 September 2007*, B. Schulte-Werning, D. Thompson, P. E. Gautier et al., Eds., Notes on Numerical Fluid Mechanics and Multidisciplinary Design, pp. 63–70, Springer, Berlin, Germany, 2008.

[16] T. Kurita, Y. Wakabayashi, H. Yamada, and M. Horiuchi, "Reduction of wayside noise from shinkansen high-speed trains," *Journal of Mechanical Systems for Transportation and Logistics*, vol. 4, no. 1, pp. 1–12, 2011.

[17] J. Y. Zhu, Z. W. Hu, and D. J. Thompson, "Analysis of aerodynamic and aeroacoustic behaviour of a simplified high-speed train bogie," in *Noise and Vibration Mitigation for Rail Transportation Systems*, J. Nielsen, Ed., pp. 489–496, Springer, Heidelberg, Germany, 2015.

[18] Y. D. Zhang, J. Y. Zhang, T. Li, and L. Zhang, "Numerical research on aerodynamic noise of trailer bogie," *Journal of Mechanical Engineering*, vol. 52, pp. 106–115, 2016.

[19] Z. S. Sun, D. L. Guo, S. B. Yao, G. W. Yang, and M. G. Li, "Identification and suppression of noise sources around high speed trains," *Engineering Applications of Computational Fluid Mechanics*, vol. 7, no. 1, pp. 131–143, 2013.

[20] N. Yamazaki, T. Takaishi, M. Toyooka, K. Nagakura, A. Sagawa, and H. Yano, "Wind tunnel tests on the control of aeroacoustic noise from high speed train," in *Noise and Vibration Mitigation for Rail Transportation Systems*, B. Schulte-Werning, D. Thompson, P. E. Gautier et al., Eds., pp. 33–39, Springer, Berlin, Germany, 2008.

[21] Y. D. Zhang, J. Y. Zhang, and T. Li, "Research on aerodynamic noise source characterization and noise reduction of high-speed trains vehicle," *Journal of the China Railway Society*, vol. 38, pp. 40–49, 2016.

[22] G. X. Cai, C. X. Xu, and Z. S. Zhang, "The progress of turbulent eddy simulation," *Aerodynamics Journal*, vol. 22, pp. 121–129, 2004.

[23] E. Garnier, N. Adams, and P. Sagaut, *Large Eddy Simulation For Compressible Flows*, Scientific Computation, Springer, Berlin, Germany, 2009.

[24] J. Y. Zhu, Z. W. Hu, and D. J. Thompson, "Flow simulation and aerodynamic noise prediction for a high-speed train wheelset," *International Journal of Aeroacoustics*, vol. 13, no. 7, pp. 533–552, 2014.

[25] P. R. Spalart, S. Deck, M. L. Shur, K. D. Squires, M. K. Strelets, and A. Travin, "A new version of detached-eddy simulation, resistant to ambiguous grid densities," *Theoretical and Computational Fluid Dynamics*, vol. 20, no. 3, pp. 181–195, 2006.

[26] M. J. Lighthill, "On sound generated aerodynamically. I: general theory," *Proceedings of the Royal Society. London. Series A. Mathematical, Physical and Engineering Sciences*, vol. 211, pp. 564–587, 1952.

[27] N. Curle, "The influence of solid boundaries upon aerodynamic sound," *Proceedings of the Royal Society of London A: Mathematical, Physical and Engineering Sciences*, vol. 231, pp. 505–514, 1955.

[28] J. E. F. Williams and D. L. Hawkings, "Sound generation by turbulence and surfaces in arbitrary motion," *Proceedings of the Royal Society of London. Series A, Mathematical and Physical Sciences*, vol. 264, pp. 321–342, 1969.

[29] J.-L. Liu, J.-Y. Zhang, and W.-H. Zhang, "Numerical analysis on aerodynamic noise of the high-speed train head," *Journal of the China Railway Society*, vol. 33, no. 9, pp. 19–26, 2011.

[30] ISO, "Acoustics-railway applications-measurement of noise emitted by railbound vehicles," ISO 3095, 2013.

[31] D. Y. Ma, *Modern Acoustic Theory Foundation*, Science Press, Beijing, China, 2004.

[32] S. B. Yao, D. L. Guo, Z. S. Sun, G. W. Yang, and D. W. Chen, "Multi-objective optimization of the streamlined head of high-speed trains based on the Kriging model," *Science China Technological Sciences*, vol. 55, pp. 3495–3509, 2012.

[33] P. Li, G. S. Tang, Y. S. Yu, and B. Lv, "Research of acoustic design for aerodynamic wind tunnel," *Journal of Experiments in Fluid Mechanics*, vol. 25, pp. 82–86, 2011.

[34] B. Zhu, G. S. Tang, G. W. Gu, and P. Li, "An investigation of background noise measurement technology in aeroacoustic wind tunnel," *Journal of Experiments in Fluid Mechanics*, vol. 23, no. 4, pp. 56–64, 2009.

[35] Z. X. Sun, J. J. Song, and Y. R. An, "Numerical simulation of aerodynamic noise generated by high speed trains," *Engineering Applications of Computational Fluid Mechanics*, vol. 6, no. 2, pp. 173–185, 2012.

[36] I. Proudman, "The generation of noise by isotropic turbulence," *Proceedings of the Royal Society. London. Series A. Mathematical, Physical and Engineering Sciences*, vol. 214, pp. 119–132, 1952.

[37] G. M. Lilley, "The radiated noise from isotropic turbulence," *Theoretical and Computational Fluid Dynamics*, vol. 6, no. 5-6, pp. 281–301, 1994.

[38] S. Sarkar and M. Y. Hussaini, "Computation of the sound generated by isotropic turbulence," Tech. Rep., Institute for Computer Applications in Science and Engineering, Hampton, Va, USA, 1993.

[39] T. Colonius, "An overview of simulation, modeling, and active control of flow/acoustic resonance in open cavities," AIAA Paper 76, 2001.

[40] N. Frémion, N. Vincent, M. Jacob, G. Robert, A. Louisot, and S. Guerrand, "Aerodynamic noise radiated by the intercoach spacing and the bogie of a high-speed train," *Journal of Sound and Vibration*, vol. 231, no. 3, pp. 577–593, 2000.

[41] C. W. Rowley, T. Colonius, and A. J. Basu, "On self-sustained oscillations in two-dimensional compressible flow over rectangular cavities," *Journal of Fluid Mechanics*, vol. 455, pp. 315–346, 2002.

[42] B. He, X. B. Xiao, Q. Zhou, Z. H. Li, and X. S. Jin, "Investigation into external noise of a high-speed train at different speeds," *Journal of Zhejiang University Science A*, vol. 15, no. 12, pp. 1019–1033, 2014.